Solar Energy Materials and Solar Cells 195 (2019) 134–141

Contents lists available at ScienceDirect

Solar Energy Materials and Solar Cells

journal homepage: www.elsevier.com/locate/solmat

Fabrication of Bi_2WO_6 photoelectrodes with enhanced photoelectrochemical and photocatalytic performance

Bandar Y. Alfaifi[a], Asif A. Tahir[a,*], K.G. Upul Wijayantha[b]

[a] Environment and Sustainability Institute (ESI), University of Exeter, Penryn Campus, Penryn, Cornwall, TR10 9FE, UK
[b] Department of Chemistry, Loughborough University, Loughborough, Leics, LE 11 3TU, UK

ARTICLE INFO

Keywords:
(Bi_2WO_6
Nanostructures
Nanoplate
Thin films
Photoelectrochemical
Photocatalyst)

ABSTRACT

Visible light active semiconductor Bi_2WO_6 photoelectrodes with desired physical and chemical properties are sought for solar energy conversion and photocatalytic applications. The porous nanostructured Bi_2WO_6 photoelectrodes are prepared by Spray Pyrolysis (SP). A detail study has been conducted to correlate the annealing temperature, morphology and crystallographic orientation with the photoelectrochemical (PEC), electrochemical and photocatalytic properties. The photoelectrodes possess an optical bandgap of 2.82 eV and exhibit anodic photocurrent. The current-voltage characterization of Bi_2WO_6 photoelectrodes reveals that the photocurrent density and photocurrent onset potential is strongly dependent on the deposition parameters. The PEC study shows that the photoelectrode annealed at 525 °C has photocurrent density of 42 μAcm^{-2} at 0.23 V (vs Ag/AgCl/3M KCl) under AM1.5 illumination and exhibit superior photocatalytic activity for Rhodamine B (RhB) degradation. The electrochemical study shows that the photoelectrode has flatband potential of 2.85 V which is in good agreement with photocurrent onset potential. This finding will have a significant influence on further exploitation of Bi_2WO_6 as a potential semiconductor material in solar energy conversion and photocatalytic applications.

1. Introduction

Architectural control of nanoparticles with well-defined shapes and alignment of nanobuilding blocks into ordered superstructures have been key challenge in materials chemistry and nanotechnology [1,2]. Recently, a significant interest has been received on controlling the shape, size and structure of nanostructured materials because of the strong correlation between morphology and physical/chemical properties [3]. Highly nanostructured materials with specific morphologies have been receiving a wide attention owing to their important role in the systematic studies of structure-property relationships [4]. Purposely designed hierarchical structures of given inorganic materials possesses novel physical and chemical properties as such structures hold the advantage of both microstructure and nanostructure [5]. For example, isotropic or anisotropic behavior and region-dependent surface reactivity are strongly related to the size, shape, and dimension of a material [6]. Traditional methods for controlling the dimension and structure are based on two strategies: one is the physical approach which includes thermal evaporation [7], physical exfoliation [8], and so on; the other is the soft chemical strategy that includes hydrothermal [9,10] surfactant [11], and molecular assemblies as soft templates [12]. Unlike the synthesis of monodispersed spherical particles, as well as one-dimension nanorods/nanowires, which have been successful in many cases, deposition of nanostructured photoelectrodes with specific properties has been shown to be much more difficult. A number of electrode deposition techniques such pulsed laser deposition [13], electrodeposition [14], spin-coating [15], dip-coating [16], spray pyrolysis [17] and chemical vapor deposition [18] have been used to obtain shape controlled single component systems.

Among different electrode/thin film deposition techniques, spray pyrolysis (SP) is simple, versatile and has advantage that a single solution source can be used to fabricate multicomponent oxide photoelectrodes. Moreover, it also diminish the stringent CVD requirement of precursor volatility and precursor need to be soluble in a solvent from which an aerosol can be generated [19,20]. Most of bismuth compounds are not easily soluble in water and common organic solvents which make it even more difficult to deposit the bismuth containing multicomponent oxide film photoelectrodes. There are published works on the preparation of Bi_2WO_6 particles by hydrothermal process and then deposition of photoelectrodes by spin coating [21], electrostatic layer by layer deposition technique [22,23] and dip-coating [24]. Recently, Mann, et al. has prepared single crystalline nanoplates of

* Corresponding author.
E-mail address: a.tahir@exeter.ac.uk (A.A. Tahir).

https://doi.org/10.1016/j.solmat.2019.02.031
Received 12 August 2018; Received in revised form 5 February 2019; Accepted 27 February 2019

Bi_2WO_6 using spray pyrolysis [25].

Bi_2WO_6 possesses very interesting intrinsic physical and chemical properties, such as ferroelectric piezoelectricity, catalytic activity and nonlinear dielectric susceptibility [26]. Recently, Bi_2WO_6 has attracted extensive attention as a potential candidate for visible-light-induced photocatalyst [15], photoelectrochemical (PEC) water splitting [27] and CO_2 reduction [28]. It is well known that the photocatalytic and PEC properties are highly depends upon particle size, morphology and structure. In early work, photocatalysts have been utilized as suspended powders [29]. However, the limitations such as low photocatalytic activity and the laborious recollection of the powder from the suspension have considerably restricted their applications. In order to overcome such obstacles, nanostructured film photoelectrodes on solid supports have been developed later. Such nanostructured photoelectrodes exhibit a large internal surface area, high porosity, and excellent photocatalytic performance. In order to study the optical, electrochemical, electronic and PEC properties, nanostructured photoelectrodes should be prepared on optically transparent conducting substrates. Unfortunately, the fabrication of highly crystalline nanostructured thin film photoelectrodes of Bi_2WO_6 on such substrates and a systematic study of PEC properties associated with nanostructure and texture have not yet been examined in detail.

Stimulated by novel properties related to nanostructures, the preparation of efficient visible-light sensitive Bi_2WO_6 photoelectrodes by systematically controlling the nanostructure and texture is the primary aim of this particular work. We also describe the preparation of highly soluble and volatile solutions containing Bi and W compounds in aqueous and organic solvents. In this work, Bi_2WO_6 nanostructured photoelectrodes with nanoplates structures are fabricated by Spray Pyrolysis (SP). These novel method is simple and reproducible route to construct nanostructured Bi_2WO_6 photoelectrodes.

Moreover, the photoelectrodes prepared in this work has shown considerably high photocurrent as well as high activity for photocatalytic degradation of Rhodamine B (RhB) dye. Our findings will undoubtedly have a significant influence on further exploitation of Bi_2WO_6 as a potential semiconductor material in solar energy conversion and photocatalytic applications.

2. Experimental

2.1. Preparation of precursor solution

Analytical grade chemicals and reagents were purchased from Sigma-Aldrich and used without further purification. Distilled water was used throughout the experiment. The solution used for the deposition of Bi_2WO_6 photoelectrodes was prepared as follows: 5.0 g of diethylenetriaminepenta-acetic acid (DTPA) and 15 mL of ammonia water (30%) were added to 300 mL of distilled water. 1.8 g of Bi_2O_3 powder and 1.0 g of $(NH_4)_6\ H_2W_{12}O_{40}{\cdot}xH_2O$ powder were added to the above stirring solution. The mixture was further stirred and heated to 80 °C in order to promote the dissolution and subsequent reaction. After 4 h of stirring, the mixture became a colorless transparent solution. The solution was evaporated to dryness under reduced pressure to eliminate any volatile by-products. The resulting powder was redissolved in 100 mL of distilled water to obtain a transparent precursor solution.

2.2. Deposition of photoelectrodes by spray pyrolysis (SP)

The Bi_2WO_6 photoelectrodes were deposited by the SP process. Fluorine doped tin oxide (FTO) glass substrates were cleaned ultrasonically (prior to spray pyrolysis) by ethanol, iso-propanol and acetone 15 min each, in that order, and then washed with de-ionized water to remove any remaining organic substances and dried with compressed air. Once cleaned the FTO glass substrate was placed in the center of a hot plate at 110 °C. The spray system comprised of a syringe pump system (New Era Pump System NE-1000), an ultrasonic atomizer nozzle (Sonozap) 1 mm diameter and a vortex attachment [30]. 10 ml of the precursor solution was sprayed on to the FTO at a rate of 1 ml min^{-1} assisted with compressed air at a rate of 3 L min^{-1}, which is passed through the vortex attachment to generate a large plume of aerosol to get a uniform coverage on the FTO. After the completion of spray, the films were further annealed at different temperatures in air.

2.3. Structural characterization

The material phase composition was determined using a Bruker D8 Advance X-ray diffractometer (XRD) (Cu Kα irradiation, 40 kV/40 mA, 0.02° 2θ step, and a scan time of 3 s per step) in the range of 20–70° 2θ. The morphology and composition of the thin film was characterized using a high resolution scanning electron microscope (SEM; HITACHI S3200N) coupled with energy dispersive spectroscopy (EDS; Oxford instrument elemental analysis).

Raman spectroscopy was undertaken using a HORIBA Jobin Yvon LabRAM HR Raman Spectrophotometer (with 632.8 nm He-Ne laser). The spectrum was recorded in the range of 100–1600 cm^{-1}.

2.4. Optical and photoelectrochemical and electrochemical characterization

Room temperature UV-Vis absorption spectra were recorded on a lambda 1050 with 150 mm integrated InGaAs sphere Perkin-Elmer UV-Vis spectrophotometer in the wavelength range of 200–800 nm. A bare FTO coated glass substrate was placed in the reference optical path, thus the absorbance measurements included only contributions from Bi_2WO_6 photoelectrodes.

A three-electrode electrochemical cell, fitted with a quartz window, was used for photoelectrochemical studies. An aqueous solution of 1M NaOH was used as the electrolyte. The potential of the Bi_2WO_6 working electrode was controlled by a potentiostat (micro-Autolab, type III). A Ag/AgCl/3M KCl electrode was used as the reference electrode and a Pt wire was adopted as the counter electrode. In electrochemical cell light enters through a quartz window and travels about a 5 mm path length in the electrolyte before illuminating the photoelectrode. The Bi_2WO_6 photoelectrode was illuminated through the electrolyte side and the illumination source was an AM1.5 class A solar simulator (Solar Light 16S–300 solar simulator).

Mott-Schottky relationship was used to calculate the flatband potential (V_{fb}) of nanostructured Bi_2WO_6 photoelectrodes. The Mott-Schottky plots were constructed using capacitance data obtained from a cyclic voltammetry (CV) technique described by Eggleston et al. [31] and Boschloo et al. [32] using the equation below.

$$c = \frac{dQ}{dV} = \frac{i\,dt}{dV} = \frac{i}{v}$$

with Q the charge, V the potential and i the current. The Cyclic voltammograms (CVs) were measured in different pH electrolytes to calculate the pH dependence of flatband potential.

3. Photocatalytic degradation of rhodamine B (RhB)

The light source for photocatalytic measurements was a 100 W ozone free Xenon lamp (Oriel LCS-100, Newport) with 420 nm high pass cut-edge filter to cut UV radiations. . Degradation of rhodamine B (RhB) was performed in a quartz cuvette reactor containing 60 ml of RhB (10 mg/L) and 1 ml of H_2O_2. The photodegradation experiment also carried out using higher concentration 20 mg/L of RhB. Prior to irradiation, the suspension was kept in the dark for 30 min to establish absorption/desorption equilibrium between RhB solution and the electrode. During the reaction, 3 mL of RhB solution was sampled at certain time intervals to check the degree of degradation, which was done by measuring the absorbance at 554 nm as a function of reaction time. After the measurement, the sampled RhB solution was returned to the reactor to keep the total volume of the reaction roughly equivalent.

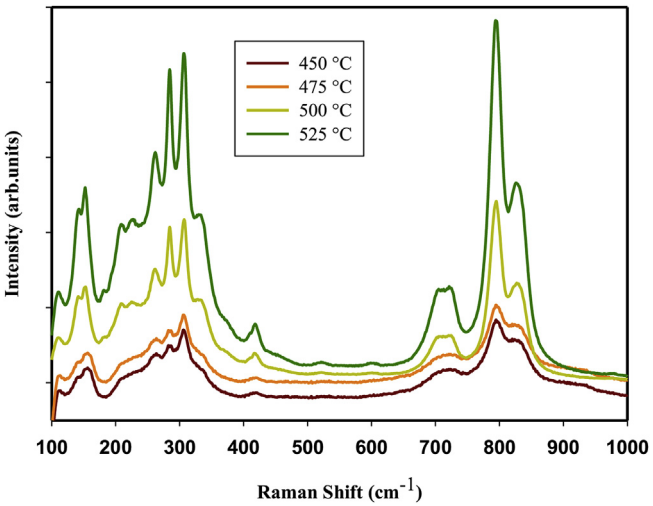

Fig. 1. Raman Spectra of Bi_2WO_6 photoelectrodes deposited by spray pyrolysis and annealed at 450 °C–525 °C.

Bi_2WO_6 photoelectrodes prepared at different calcination temperature were used in the experiment in order to investigate the influence of annealing temperature of electrodes on the efficiency of degradation.

4. Result and discussion

Nanostructured Bi_2WO_6 photoelectrodes were successfully prepared through a simple procedure employing SP processes. A comparative study of the effect of annealing/deposition temperature on the morphology and PEC properties of the photoelectrodes was conducted. In general, photoelectrodes deposited in the present work are superior to the ones reported in the literature in terms of their easy fabrication (one-step process, clean deposition, good adhesion to FTO substrate as verified by "Scotch Tape Test") and PEC performance. The photoelectrodes are also highly stable under PEC and electrochemical measurement conditions.

4.1. Structural characterization

Raman spectra of as-prepared photoelectrodes are shown in Fig. 1. The peaks in the range of 600–1000 cm^{-1} are assigned to the stretches of the W–O bands, according to the Grane et al. [33] The bands at 760 and 790 cm^{-1} of Bi_2WO_6 were associated with the antisymmetric and symmetric A_g modes of terminal O–W–O chain. The band of 310 cm^{-1}

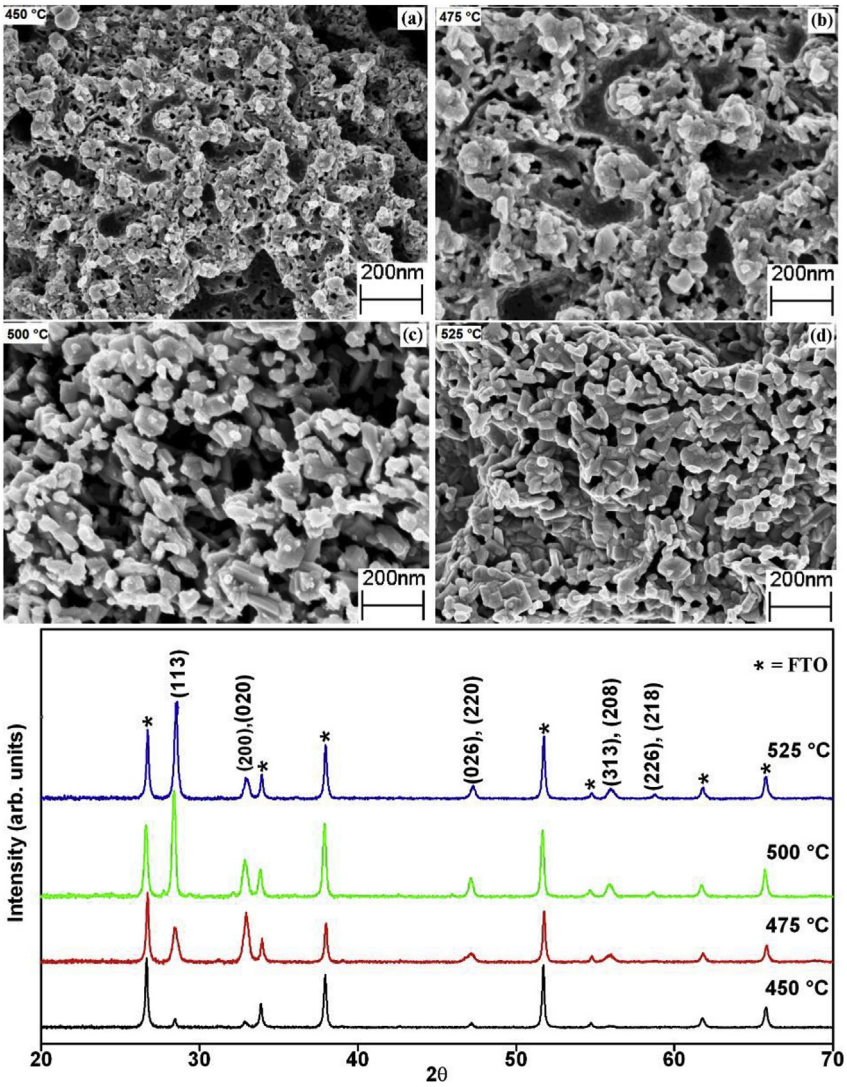

Fig. 2. The XRD peak pattern and SEM micrographs (a–d) of photoelectrodes deposited by SP and annealed at 450–525 °C.

could be assigned to translational modes involving simultaneous motions of Bi^{3+} and WO_4. The bands at about 300 cm^{-1} were assigned to the modes of terminal WO_2 group. The W–O bonds of intermediate length (about unit valency) are characteristic of bridging W–O bonds and are assigned to Raman mode stretching wavenumbers in the range of 700–1000 cm^{-1} [34]. As can be seen in Fig. 1, the intensity of peaks increase with the increase in annealing temperature indicate that the crystallinity of photoelectrode increase with temperature. These observations are in good agreement with SEM and XRD results.

4.2. Effect of annealing temperature on crystallinity and morphology

The effect of precursor solution and different annealing/deposition temperature on the nanostructure and morphology of Bi_2WO_6 photoelectrodes prepared by SP were investigated in detail. In order to study the effect of substrate temperature on crystallinity and morphology, photoelectrodes were annealed on different substrate temperatures while all other parameters were kept constant. The effect of annealing temperature on properties of photoelectrodes prepared by SP was studied over the temperature range of 450–525 °C.

The phase and crystallinity of photoelectrodes were characterized by XRD and all peaks indexed by (*) in XRD peak pattern correspond to the substrate fluorinated SnO_2 layer, while the remaining reflections were indexed to orthorhombic phase (Russellite) Bi_2WO_6 with space group B2ab (Fig. 2). The peak pattern is in good agreement with the reported data for Bi_2WO_6 (ICDD 01-073-2020, a = 5.457 Å, b = 5.436 Å, and c = 16.425 Å) [35]. The Fig. 2 illustrates the effect of annealing temperature on electrode structure and morphology. The XRD peak pattern showed that the Bi_2WO_6 phase was achieved at 450 °C with very small peak intensities which may be due to poor crystallinity. The peak intensity increased with the increase in annealing temperature indicating the enhanced crystallinity of photoelectrodes. The crystallites size calculated from the boarding of the (113) peak of the electrode annealed at 525 °C is 65 nm.

The analysis of SEM images shows that the photoelectrodes annealed at 450 °C consist of big lumps with very uniform pores as shown in SEM Fig. 2a. With the increase of temperature, the lumps began to disperse and particles with different boundaries starts emerging. The growth of particles with specific shape became more apparent with the increase of annealing temperature as elucidated by progressive SEM images (Fig. 2b and c). The particles acquired a near cuboids shape after annealing at 525 °C as shown in SEM image (Fig. 2d). These Bi_2WO_6 particles have a length of about 100–150 nm and a thickness of about 50–70 nm and are linked together to make a porous structured electrode.

4.3. Optical characterization

In Bi_2WO_6, Bi^{+3} has two 6s valence electrons in the crystalline phase. The band structure of Bi_2WO_6 was suggested to be composed of W5d (conduction band, CB) and hybridization of Bi6s and O2p (valence band, VB) [36]. It has been reported that Bi_2WO_6 thin films have a steep absorption edge in the visible range, indicating that it is due to the intrinsic transition within the material related to the fundamental absorption edge rather than the transition from impurity levels [37].

The optical properties of Bi_2WO_6 samples were recorded using UV/Vis spectroscopy. Fig. 3 shows direct bandgap [38,39] of thin films for Bi_2WO_6 film photoelectrodes for porous nanoplate electrode deposited by SP at 525 °C. For a crystalline semiconductor, it was shown that the optical absorption near the band edge follows the equation $(\alpha h\nu)^n = A(h\nu - E_g)$, where α, ν, E_g, and A are light absorption coefficient, frequency, bandgap, and a constant, respectively. Among them, n decides the characteristics of the transition in a semiconductor. A slight increase in absorption is observed with increase in annealing temperature and absorption spectra are given in Fig. S2. As seen from Fig. S2, the absorption of Bi_2WO_6 does not show a clear absorption edged.

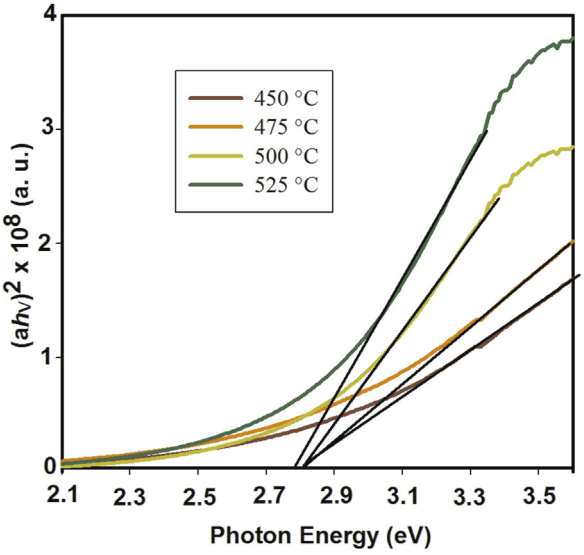

Fig. 3. Plot of $(ah\upsilon)^2$ versus photon energy ($h\upsilon$) for Bi_2WO_6 photoelectrodes deposited by spray pyrolysis and annealed at 450 °C–525 °C.

This can be due to very thin films as well as due to large voids and high porosity in the photoelectrodes. The absorption is directly used as equivalent to the absorption coefficient in determination of bandgaps. The annealing temperature has slight effect on bandgap (E_g) and the bandgap estimated by extrapolation of the plots of $(ah\nu)^2$ versus $h\nu$ are 2.82 eV (Fig. 3) and are comparable to the reported values for Bi_2WO_6 powder nanoparticles [4].

4.4. Photoelectrochemical properties

The photoelectrochemical (PEC) properties of Bi_2WO_6 photoelectrodes were investigated under AM 1.5 illumination in a 3-electrodes open quartz cell. The steady-state J-V plots in Fig. 4a show the dependence of photocurrent density on the annealing temperature. The photocurrent increases with the increase of annealing temperature. The crystallite size, orientation and morphology of the photoelectrodes drastically varied with the annealing temperature. Further increased of annealing temperature could not be continued beyond certain limit due to instability of glass substrate at high temperature (> 550 °C). The result indicate that the morphology as well as the degree of crystallographic preferred orientation are the key factors in defining the light harvesting and charge transfer properties [40].

The photocurrent increased rapidly with the applied potential, which could be due to fact that the high internal surface area exposed to the electrolyte provides a large effective semiconductor/electrolyte interface. Thus, the separation of photogenerated carriers within the width of the space charge layer becomes a key factor to enhance PEC performance of photoelectrodes.

The best photoelectrodes prepared using the SP methods have been studied under chopped light (AM 1.5 illumination) to reveal the dark current simultaneously. Fig. 4b describes the photocurrent transients in the potential range that encompasses the photocurrent and dark current onset potentials. For comparison, the steady-state J-V plot was superimposed on the transient plot in each case. Steady-state and transient J-V plots agree well for all photoelectrodes. Generally dark current starts at about 0.6 V (vs. Ag/AgCl/3M KCl) in 1M NaOH electrolyte. This photoelectrode have shown about 42 μAcm^{-2} photocurrent density at 0.23 V (vs Ag/AgCl/3M KCl) under AM1.5 illumination and a negligible dark current (Fig. 4b). However, the recombination characteristics are evident in photocurrent transients. This indicates that the light harvesting properties of Bi_2WO_6 photoelectrodes depend on the fabrication conditions which are directly related to the texture, morphology and

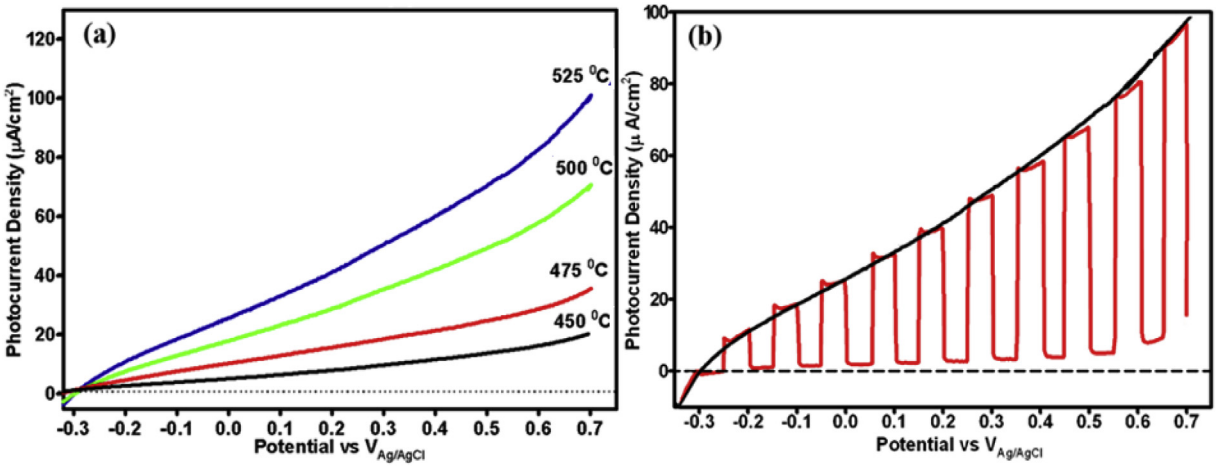

Fig. 4. (a) J-V plots showing the dependence of photocurrent on annealing temperature for the photoelectrodes (b) Chopped and steady state J-V plot of porous nanostructured annealed at 525 °C.

preferred orientation of photoelectrodes [41].

4.5. Electrochemical characterization

One of the important parameters in the study of semiconductor electrolyte interface is flat-band potential which explains the electrochemical characteristics of the system in dark and under illumination. Cyclic voltammograms of Bi_2WO_6 photoelectrodes are measured in three electrodes mode under dark condition at different scan rates in different pH electrolytes. The potential range is such that the Bi_2WO_6 photoelectrodes are always under depletion conditions; i.e., the applied potential is more negative than the flatband potential (V_{fb}). An intriguing feature of these CVs is that the current is an approximately linear function of the applied potential, in the directions of both the forward and the reverse scans. Furthermore, the current at a given potential is linearly dependent on the scan rate. The cyclic voltammograms recorded as a function of scan rate for Bi_2WO_6 photoelectrodes annealed at 525 °C are shown in Fig. S3. The CVs of Bi_2WO_6 photoelectrodes prepared in the current work do not shows any electrochemical interfacial redox reactions indicates that the origin of current is capacitive.

In the absence of interfacial redox reactions, the scan-rate (n) dependence of current can be attributed to charging and discharging of the space charge layer. The CVs collected for a series of scan rates, the current (i) was plotted versus scan rate (n) at selected applied potential. The current i was plotted against scan rate v at selected applied potentials (both anodic and cathodic plots were given in Fig. S4. The slope of the line in such a plot is a measure of space charge layer capacitance (C_{SC}) at each potential. The data from the forward scans of the CVs are used to calculate the capacitance to construct the Mott − Schottky plots (i.e., C^{-2} vs V) and the flatband potential was estimated by extrapolating the linear part of the Mott − Schottky plots. The Mott − Schottky plot determined at pH 13.3 for the photoelectrode is given in Fig. 5. The flatband potential 2.85 V estimated from the Mott − Schottky plot remarkably agrees with the photocurrent onset potentials which further support the negative shift of the photocurrent onset associated with hierarchical microsphere structures.

It is well known that the flatband potential of many semiconductors in contact with aqueous electrolytes depends on the pH of the solution. The relationship between V_{fb} and the pH was linear with a slope of about 60 mV per pH unit (Fig. 5 inset), which is very close to the Nernstian response (−59 mV/pH) expected for reactions involving protons and hydroxide ions.

However, this relationship deviates from the Nernstian slope for the electrodes annealed at 450 °C and 475 °C is more pronounced especially at pH 9 and 10 as shown in Fig. S5. This deviation can be attributed to the microstructure and crystallinity of the electrodes. The electrode annealed at 450 °C and 475 °C has bigger voids but the individual particle is not crystalline with clear boundaries. However, with the increase in temperature the particles become more crystalline and voids become more distributed making films more porous and crystalline. The electrode annealed at 500 °C and 525 °C follow the Nernstian slope to entire range of measured pH particularly and the V_{fb} and its pH dependence support the argument that the nanoplate structures provides high internal surface area which allows more electrolyte solution to penetrate to the interior of each porous nanostructure providing a large semiconductor/electrolyte interface to enhance the photoelectrochemical and photocatalytic performance of photoelectrodes.

4.6. Photocatalytic activity

The photocatalytic activity of Bi_2WO_6 film has been evaluated by degredtion of rhodamine B (RhB) as the target pollutant. The RhB degradation is tested for 10 mg/L and 20 mg/L RhB concentration. Fig. 6 shows the photocatalytic degradation of RhB (10 mg/L) over Bi_2WO_6 prepared at different calcination tempreture, 525 °C, 500 °C, 475 °C, and 450 °C. The photocatalytic results for RhB (20 mg/L) is given in supporting information Fig. S6 and Fig. S7. It can be seen from Fig. 6a that, maximum degredation of RhB is achived in 30min for the film annealed at 525 °C. It is also be noted, the minimum photocatalytic activity is obtained by the film annealed at 450 °C as shown in Fig. 6d. Fig. 7 shows the photocatalytic activity of Bi_2WO_6 films prepared at different tempreture at the wavelength of 554 nm as a function of C/C_o *vs.* irradiation time.

The primary degradation reaction is estimated to follow a pseudo first-order kinetic law, according the Equation (1).

$$-Ln\frac{C}{C_0} = k_{app}\,t \tag{1}$$

Where k_{app} is the apparent pseudo-first-order reaction is rate constant and reaction time is t. The Ln(C/C_0) was replotted as a function of illumination time for RhB shown in Fig. 8. From the straight lines obtained in Fig. 8 which confirm kinetics of RhB degradation followed the pseudo first-order degradation curve, which agreed with the Langmuir–Hinshelwood L-H model [42].

The rate constant for photoelectrodes annealed at different temperature is determined from the slope of the plots in Fig. 8. The photocatalytic kinetic parameters such as pseudo-first-order rate constant and substrate half-life are shown in Table 1. The parameters in Table 1 confirm that an increase in the annealing temperature leads to increase in the rate of degradation of RhB by Bi_2WO_6 films. It is obsereved that

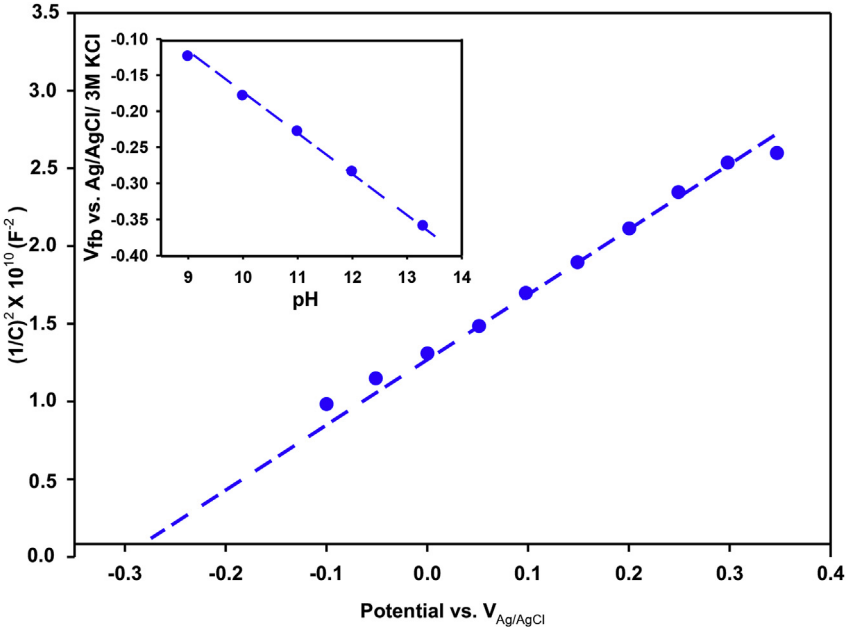

Fig. 5. Mott – Schottky plot constructed using capacitance data calculated from slope of anodic lines of current vs. scan rate at each potential measured at pH 13.3 for Bi_2WO_6 photoelectrodes annealed at 525 °C while inset shows pH dependence of the flatband potential (V_{fb}) for Bi_2WO_6 photoelectrode.

calcination temperature has significant impact on the photocatalytic activity of as-prepared films. The increase in the annealing temperature lead to increase the crystallinity which provide better surface area which is the main reason for the enhancement of the photocatalytic activity [43,44]. The dye degradation study prove that the light harvesting performance is directly related to the texture, morphology and preferred orientation of photoelectrodes.

5. Conclusion

We have demonstrated a convenient single solution source spray pyrolysis process for the fabrication of Bi_2WO_6 photoelectrodes with different annealing temperature. The fabrication method and annealing temperature have strong influence on the texture, morphology and orientation of Bi_2WO_6 photoelectrodes. These photoelectrodes are highly reproducible and possess an optical bandgap of ~2.8 eV and exhibit anodic photocurrent. The present work opens new routes to improve the properties of Bi_2WO_6 photoelectrodes by controlling their texture, morphology and orientation. Overall, the methods reported here provide simple and convenient means for modulation of the surface properties of Bi_2WO_6 photoelectrodes. We believe that our findings will trigger exploitation of Bi_2WO_6 photoelectrodes in a wide range of areas such as photocatalytic, electrochemical, photoelectrochemical and electronic applications.

Acknowledgements

We would like to acknowledge The Saudi Arabian Cultural Bureau

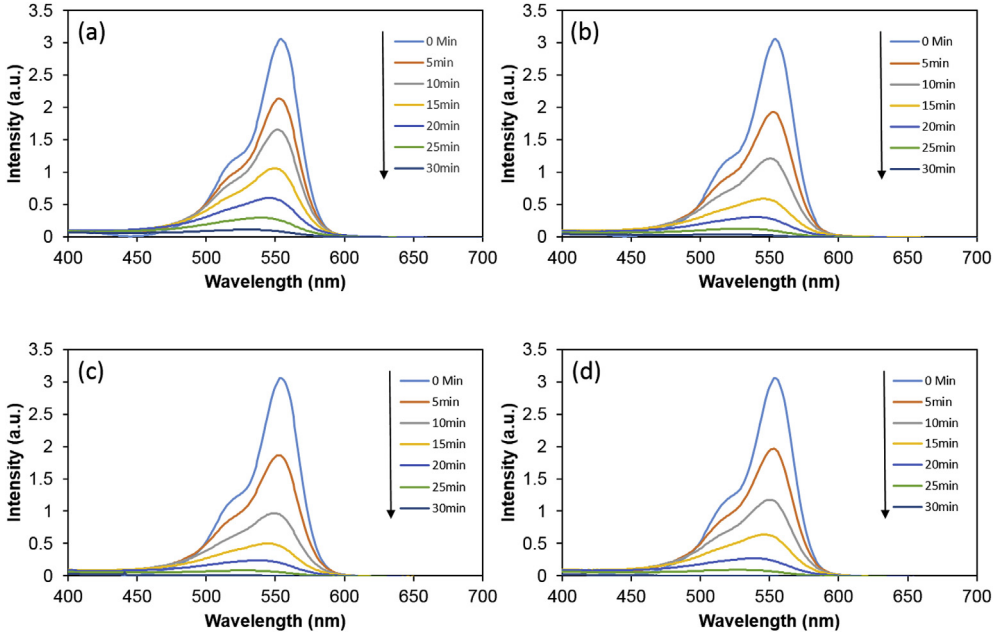

Fig. 6. Photocatalytic degredation of RhB over Bi_2WO_6 prepared at different calcination tempreture, (a) 525 °C, (b) 500 °C, (c) 475 °C, (d) 450 °C.

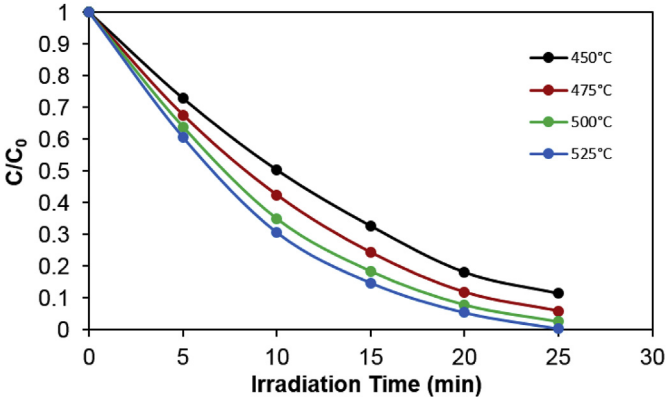

Fig. 7. The plot of C/C_0 *vs.* the irradiation time of Bi_2WO_6 films prepared at different calcination tempreture.

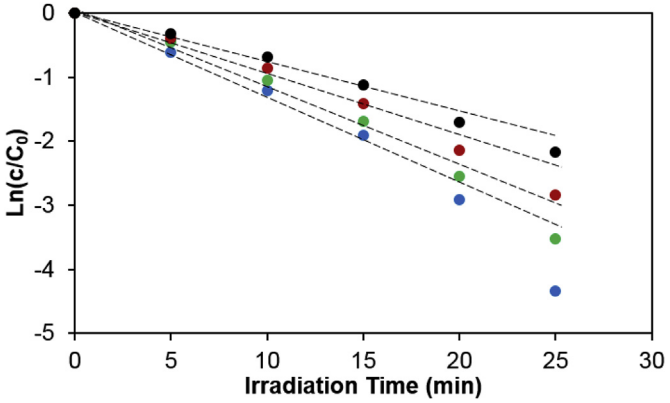

Fig. 8. Kinetic plot of $Ln(C/C_0)$ *vs.* the irradiation time for the photocatalytic degradation of rhodamine B by Bi_2WO_6 films prepared at different calcination temperature.

Table 1
Apparent constant and half-life for Langmuir-Hinshel-wood model for rhodamine B photo degradation by Bi_2WO_6 films.

Temperature (°C)	k_{app}(min^{-1})	$t_{1/2}$ (min)
450°C	0.116	11
475°C	0.138	7
500°C	0.157	6
525°C	0.180	5

(SACB) for providing PhD fellowship to Bandar Y. Alfaifi. The financial support was provided by Engineering and Physical Sciences Research Council (EPSRC), UK under the research grant No EP/P510956/1 and EP/R512801/1. We also acknowledge UKIERI-DST2016-17-0089 project for partly funding the present work. NSG Pilkington Glass Ltd. is acknowledged for kindly providing the FTO substrates for this work.

Appendix A. Supplementary data

Supplementary data to this article can be found online at https://doi.org/10.1016/j.solmat.2019.02.031.

References

[1] F. Amano, K. Nogami, B. Ohtani, Visible light-responsive bismuth tungstate photocatalysts: effects of hierarchical architecture on photocatalytic activity, J. Phys. Chem. C 113 (2009) 1536–1542.
[2] L. Zhang, Y. Zhu, A review of controllable synthesis and enhancement of performances of bismuth tungstate visible-light-driven photocatalysts, Catal. Sci. Technol. 2 (2012) 694–706.
[3] D. Whang, S. Jin, Y. Wu, C.M. Lieber, Large-scale hierarchical organization of nanowire arrays for integrated nanosystems, Nano Lett. 3 (2003) 1255–1259.
[4] L. Zhang, W. Wang, L. Zhou, H. Xu, Bi_2WO_6 nano-and microstructures: shape control and associated visible-light-driven photocatalytic activities, Small 3 (2007) 1618–1625.
[5] Y. Wang, Q. Zhu, H. Zhang, Fabrication and magnetic properties of hierarchical porous hollow nickel microspheres, J. Mater. Chem. 16 (2006) 1212–1214.
[6] J. Huang, A.R. Tao, S. Connor, R. He, P. Yang, A general method for assembling single colloidal particle lines, Nano Lett. 6 (2006) 524–529.
[7] C. Liang, Y. Shimizu, T. Sasaki, H. Umehara, N. Koshizaki, Au-mediated growth of wurtzite ZnS nanobelts, nanosheets, and nanorods via thermal evaporation, J. Phys. Chem. B 108 (2004) 9728–9733.
[8] U.K. Gautam, S. Vivekchand, A. Govindaraj, G. Kulkarni, N. Selvi, C. Rao, Generation of onions and nanotubes of GaS and GaSe through laser and thermally induced exfoliation, J. Am. Chem. Soc. 127 (2005) 3658–3659.
[9] Y. Tian, B. Chang, J. Lu, J. Fu, F. Xi, X. Dong, Hydrothermal synthesis of graphitic carbon nitride–Bi2WO6 heterojunctions with enhanced visible light photocatalytic activities, ACS Appl. Mater. Interfaces 5 (2013) 7079–7085.
[10] C. Yang, Y. Huang, F. Li, T.J.J.o.m.s. Li, One-step Synthesis of Bi_2WO_6/TiO_2 Heterojunctions with Enhanced Photocatalytic and Superhydrophobic Property via Hydrothermal Method ,51 (2016), pp. 1032–1042.
[11] S. Chen, Z. Fan, D.L. Carroll, Silver nanodisks: synthesis, characterization, and self-assembly, J. Phys. Chem. B 106 (2002) 10777–10781.
[12] Y. Li, J. Liu, X. Huang, G. Li, Hydrothermal synthesis of Bi_2WO_6 uniform hierarchical microspheres, Cryst. Growth Des. 7 (2007) 1350–1355.
[13] Y. Ahn, J.Y. Son, Ferroelectric properties of highly c-oriented epitaxial Bi2WO6 thin films, J. Cryst. Growth 462 (2017) 41–44.
[14] J. Safaei, H. Ullah, N.A. Mohamed, M.F.M. Noh, M.F. Soh, A.A. Tahir, N.A. Ludin, M.A. Ibrahim, W.N.R.W. Isahak, M.A.M. Teridi, Enhanced photoelectrochemical performance of Z-scheme g-C_3N_4/$BiVO_4$ photocatalyst, Appl. Catal. B Environ. 234 (2018) 296–310.
[15] C. Sun, Y. Wang, Q. Su, Sol-gel synthesis of Bi_2WO_6/graphene thin films with enhanced photocatalytic performance for nitric monoxide oxidation under visible light irradiation, Chem. Phys. Lett. 702 (2018) 49–56.
[16] Z. Du, R. Guo, J. Lan, S. Jiang, C. Cheng, L. Zhao, L. Peng, Preparation and photocatalytic activity of bismuth tungstate coated polyester fabric, Fibers Polym. 18 (2017) 2212–2218.
[17] Y. Huang, Z. Ai, W. Ho, M. Chen, S. Lee, Ultrasonic spray pyrolysis synthesis of porous Bi_2WO_6 microspheres and their visible-light-induced photocatalytic removal of NO, J. Phys. Chem. C 114 (2010) 6342–6349.
[18] K. Ishikawa, T. Watanabe, H. Funakubo, Preparation of Bi_2WO_6 thin films by metalorganic chemical vapor deposition and their electrical properties, Thin Solid Films 392 (2001) 128–133.
[19] J.S. Sagu, K. Wijayantha, A.A. Tahir, The pseudocapacitive nature of $CoFe_2O_4$ thin films, Electrochim. Acta 246 (2017) 870–878.
[20] A.A. Tahir, K.U. Wijayantha, Photoelectrochemical water splitting at nanostructured $ZnFe_2O_4$ electrodes, J. Photochem. Photobiol. A Chem. 216 (2010) 119–125.
[21] J. Li, X. Zhang, Z. Ai, F. Jia, L. Zhang, J. Lin, Efficient visible light degradation of rhodamine B by a photo-electrochemical process based on a Bi_2WO_6 nanoplate film electrode, J. Phys. Chem. C 111 (2007) 6832–6836.
[22] S. Zhang, J. Shen, H. Fu, W. Dong, Z. Zheng, L. Shi, Bi_2WO_6 photocatalytic films fabricated by layer-by-layer technique from Bi2WO6 nanoplates and its spectral selectivity, J. Solid State Chem. 180 (2007) 1456–1463.
[23] D. Kang, Y. Park, J.C. Hill, K.S. Choi, Preparation of Bi-based ternary oxide photoanodes $BiVO_4$, Bi_2WO_6, and $Bi_2Mo_3O1_2$ using dendritic Bi metal electrodes, 5 (2014) 2994–2999.
[24] X. Zhao, Y. Wu, W. Yao, Y. Zhu, Photoelectrochemical properties of thin Bi_2WO_6 films, Thin Solid Films 515 (2007) 4753–4757.
[25] A.K. Mann, S.E. Skrabalak, Synthesis of single-crystalline nanoplates by spray pyrolysis: a metathesis route to Bi_2WO_6, Chem. Mater. 23 (2011) 1017–1022.
[26] N. Kim, R.-N. Vannier, C.P. Grey, Detecting different oxygen-ion jump pathways in Bi_2WO_6 with 1-and 2-dimensional 17O MAS NMR spectroscopy, Chem. Mater. 17 (2005) 1952–1958.
[27] G. Dong, Y. Zhang, W. Wang, L. Wang, Y. Bi, Facile fabrication of nanoporous Bi_2WO_6 photoanodes for efficient solar water splitting, Energy Technol. 5 (2017) 1912–1918.
[28] Z. Jiang, X. Liang, H. Zheng, Y. Liu, Z. Wang, P. Wang, X. Zhang, X. Qin, Y. Dai, M.-H. Whangbo, Photocatalytic reduction of CO_2 to methanol by three-dimensional hollow structures of Bi_2WO_6 quantum dots, Appl. Catal. B Environ. 219 (2017) 209–215.
[29] J. Li, J. Zhou, H. Hao, W. Li, G. Liu, Exposed specific (040) and (110) facets of $BiVO_4$ modified with Bi_2WO_6 nanoparticles for enhanced photocatalytic performance, New J. Chem. 41 (2017) 6922–6927.
[30] G.S. Pawar, A.A. Tahir, Unbiased spontaneous solar fuel production using stable $LaFeO_3$ photoelectrode, Sci. Rep. 8 (2018) 3501.
[31] C.M. Eggleston, A.J. Shankle, A.J. Moyer, I. Cesar, M. Grätzel, Anisotropic photocatalytic properties of hematite, Aquat. Sci. 71 (2009) 151–159.
[32] G. Boschloo, D. Fitzmaurice, Spectroelectrochemistry of highly doped nanostructured tin dioxide electrodes, J. Phys. Chem. B 103 (1999) 3093–3098.
[33] M. Crane, R.L. Frost, P.A. Williams, J. Theo Kloprogge, Raman spectroscopy of the molybdate minerals chillagite (tungsteinian wulfenite-I4), stolzite, scheelite, wolframite and wulfenite, J. Raman Spectrosc. 33 (2002) 62–66.
[34] M. Maczka, L. Macalik, K. Hermanowicz, L. Kępiński, P. Tomaszewski, Phonon properties of nanosized bismuth layered ferroelectric material—Bi_2WO_6, J. Raman Spectrosc. 41 (2010) 1059–1066.

[35] D. Ma, S. Huang, W. Chen, S. Hu, F. Shi, K. Fan, Self-assembled three-dimensional hierarchical umbilicate Bi_2WO_6 microspheres from nanoplates: controlled synthesis, photocatalytic activities, and wettability, J. Phys. Chem. C 113 (2009) 4369–4374.
[36] H. Fu, L. Zhang, W. Yao, Y. Zhu, Photocatalytic properties of nanosized Bi_2WO_6 catalysts synthesized via a hydrothermal process, Appl. Catal. B Environ. 66 (2006) 100–110.
[37] A. Kudo, I. Tsuji, H. Kato, $AgInZn_7S_9$ solid solution photocatalyst for H_2 evolution from aqueous solutions under visible light irradiation, Chem. Comm. (2002) 1958–1959.
[38] Y. Zhou, X. Meng, L. Tong, X. Zeng, X.J.E. Chen, Template-free Fabrication of Bi_2WO_6 Hierarchical Hollow Microspheres with Visible-Light-Driven Photocatalytic Activity , 9 (2016), p. 764.
[39] F. Ren, J. Zhang, Y.J.R.A. Wang, Enhanced Photocatalytic Activities of Bi_2WO_6 by introducing Zn to replace Bi lattice sites: a first-principles study, 5 (2009) 29058–29065.
[40] B. Yang, Y. Zhang, E. Drabarek, P.R. Barnes, V. Luca, Enhanced photoelectrochemical activity of sol-gel tungsten trioxide films through textural control, Chem. Mater. 19 (2007) 5664–5672.
[41] L.W. Zhang, Y.J. Wang, H.Y. Cheng, W.Q. Yao, Y.F. Zhu, Synthesis of porous Bi_2WO_6 thin films as efficient visible-light-active photocatalysts, Adv. Mater. 21 (2009) 1286–1290.
[42] C.S. Turchi, D.F.J.J.o.c. Ollis, Photocatalytic degradation of organic Water contaminants: mechanisms involving hydroxyl radical attack, 122 (1990) 178–192.
[43] J.-G. Yu, H.-G. Yu, B. Cheng, X.-J. Zhao, J.C. Yu, W.-K. Ho, The effect of calcination temperature on the surface microstructure and photocatalytic activity of TiO_2 thin films prepared by liquid phase deposition, J. Phys. Chem. B 107 (2003) 13871–13879.
[44] R. De, S.M. Haque, S. Tripathi, K.D. Rao, R. Singh, T. Som, N. Sahoo, Temperature dependent optical characterization of Ni-TiO_2 thin films as potential photocatalytic material, AIP Adv. 7 (2017) 095115.